IEEE Access
Multidisciplinary ⋮ Rapid Review ⋮ Open Access Journal

Received 10 August 2022, accepted 7 September 2022, date of publication 21 September 2022,
date of current version 29 September 2022.

Digital Object Identifier 10.1109/ACCESS.2022.3208350

RESEARCH ARTICLE

Dental-YOLO: Alveolar Bone and Mandibular Canal Detection on Cone Beam Computed Tomography Images for Dental Implant Planning

MONICA WIDIASRI[1,2], (Member, IEEE), AGUS ZAINAL ARIFIN[1], NANIK SUCIATI[1], (Member, IEEE), CHASTINE FATICHAH[1], (Member, IEEE), EHA RENWI ASTUTI[3], RARASMAYA INDRASWARI[4], (Member, IEEE), RAMADHAN HARDANI PUTRA[3], AND CHOIRU ZA'IN[5]

[1]Department of Informatics, Faculty of Intelligent Electrical and Informatics Technology, Institut Teknologi Sepuluh Nopember, Surabaya 60111, Indonesia
[2]Department of Informatics, Faculty of Engineering, Universitas Surabaya, Surabaya 60293, Indonesia
[3]Department of Dentomaxillofacial Radiology, Faculty of Dental Medicine, Universitas Airlangga, Surabaya 60131, Indonesia
[4]Department of Information Systems, Faculty of Intelligent Electrical and Informatics Technology, Institut Teknologi Sepuluh Nopember, Surabaya 60111, Indonesia
[5]Faculty of Information Technology, Monash University, Clayton, VIC 3800, Australia

Corresponding author: Nanik Suciati (nanik@if.its.ac.id)

This work was funded by the Directorate General of Higher Education, Ministry of Education and Culture of the Republic of Indonesia for Doctoral Dissertation Research (PDD) 2020–2021 under Grant 008/E5/PG.02.00.PT/2022 and supported by the University of Surabaya for a Doctoral Program Scholarship under Grant 1151/PKD-SL/SDM/VIII/2020.

ABSTRACT In planning a mandibular posterior dental implant, identifying the exact location of the alveolar bone (AB) and mandibular canal (MC) is essential to determine the height and width of the available bone. Cone beam computed tomography (CBCT) is a 3D imaging modality widely used for dental implant planning, which requires a lower radiation dose compared to medical CT and can provide cross-sectional image quality to visualize AB and MC. The radiologist carried out the AB and MC detection processes manually on each section of the CBCT image until the appropriate area was determined for bone measurement. This process is time consuming, and the measurement accuracy depends on the ability and experience of the radiologist. This study proposes an automatic and simultaneous detection system for AB and MC based on 2D grayscale CBCT images, that can simplify and expedite dental implant planning. We introduce Dental-YOLO, an efficient version of YOLOv4 specifically developed to detect AB and MC, with two-scale feature maps at low and high scales. The height and width of the available bone in the implant area were estimated by using the detected bounding box attributes. The AB and MC detection performances using Dental-YOLO reached a mean average precision of 99.46%. The two-way analysis of variance (ANOVA) test showed no difference in the bone height and width measurements produced by the proposed approach and manual measurement by radiologists. Our results suggest that the Dental-YOLO detection system could be helpful for dental implant surgery and presurgical treatment planning.

INDEX TERMS Alveolar bone, CBCT, bone measurement, dental implant planning, mandibular canal, object detection, YOLO.

I. INTRODUCTION

Dental implants are artificial tooth roots implanted in the jaw-bone to replace the lost teeth. Presurgical treatment planning is required to determine the ideal implant dimension and position to ensure long-term success and reduce the risks associated with dental implant surgery. Cone beam computed tomography (CBCT) has been widely used in implant dentistry because of its advantages in providing anatomical information as well as three-dimensional (3D) images of

The associate editor coordinating the review of this manuscript and approving it for publication was Essam A. Rashed.

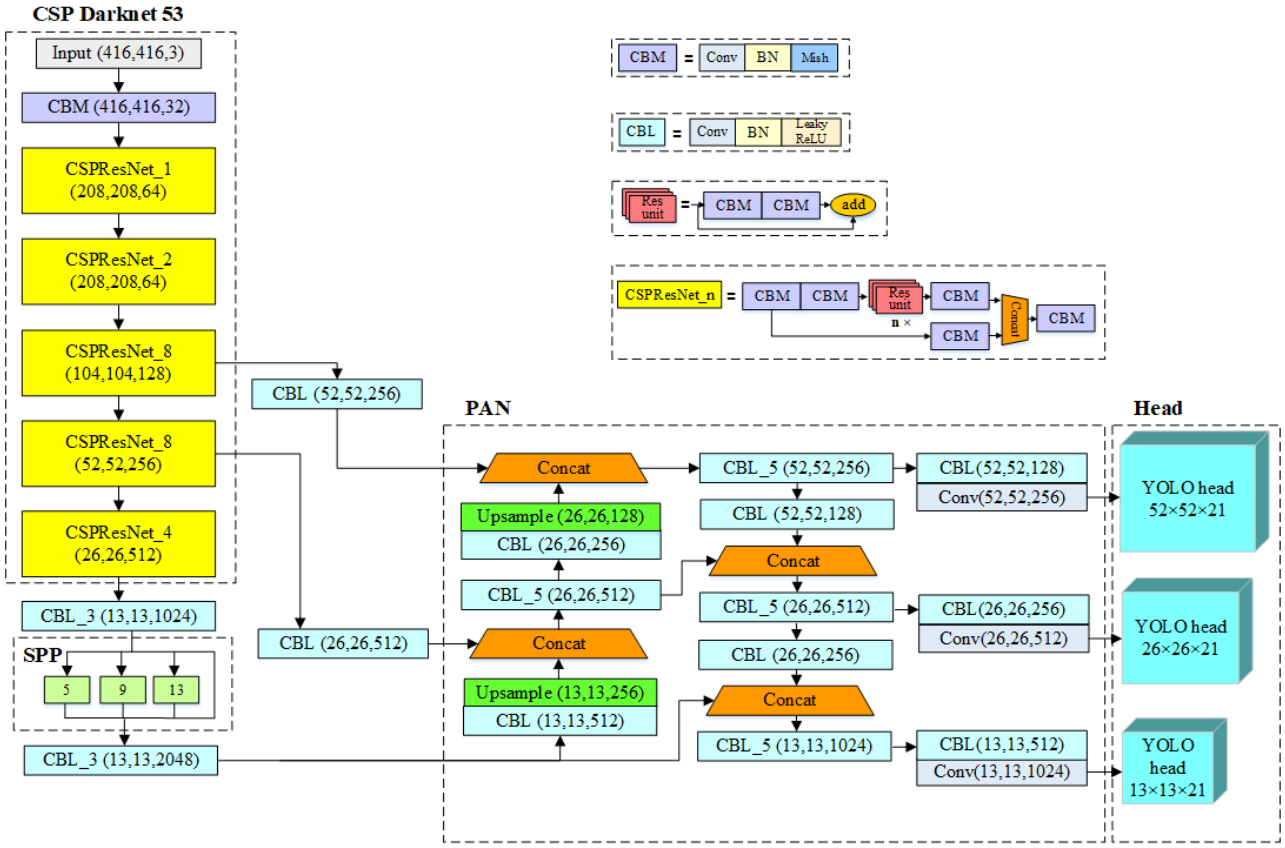

FIGURE 1. YOLOv4 architecture.

roots [1], bones [1], [2], nerves [1], and crucial structures in the implantation site [1], [2]. Thus, CBCT helps in dental implant planning to improve treatment outcomes by providing essential information on ideal implant dimensions and positions according to the available bone [3].

Dental implant placement in the mandibular posterior site should consider the location of the mandibular canal (MC) as a crucial structure [4], [5]. The MC was identified manually in each cross-section of the CBCT images, followed by manual bone height and width measurements by a radiologist using a 3D imaging software. The width and height of the alveolar bone (AB) are essential for determining the implant dimensions. Identifying the MC and measuring the bone is time-consuming and labor-intensive. Furthermore, the accuracy of the measurement depends on the radiologist's expertise and experience in interpreting CBCT images [6], [7].

Deep learning has progressed rapidly and has achieved significantly higher accuracy than traditional machine learning because it can extract high-dimensional features automatically [8]. Deep learning-based approaches can significantly reduce the time and mistakes carried out by inexperienced radiologists in interpreting the medical images in their daily clinical practice. The deep learning approach was initially implemented in dental radiology research [9]. Deep learning has been used to successfully detect bone radiography levels in panoramic radiographs [10], localize the MC on CBCT volume [6], classify teeth on CBCT images [11], segment AB on CBCT images [12], segment the mandibular cortical bone [13], MC [14], [15], tooth [12], [16], [17], and inferior alveolar nerve [18] on CBCT images.

Mandibular dental implant planning requires detection or segmentation of the AB and MC. Cui *et al.* proposed automatic tooth and alveolar bone segmentation on 3D CBCT images using the V-Net method which is a 3D fully CNN [12]. The accuracy of the alveolar bone segmentation in that study reached a Dice value of 94.5%. Research on alveolar bone segmentation with a deep learning approach that uses CBCT images has not been done much. Opportunities are available to conduct studies on AB segmentation using CBCT images. Jaskari *et al.* proposed a deep learning approach to automatically locate MC in CBCT images using a 3D fully CNN [6]. The MC localization accuracy was 0.90. The result can reduce the manual process of annotating MC. Kwak *et al.* proposed a deep learning approach based on two-dimensional (2D) SegNet, 2D U-Nets, and 3D U-Nets to automatically segment the MC on CBCT images [14]. Experiments with training using pre-training weights showed better segmentation results, and the segmentation accuracy of 3D U-Net model was the best, with a global accuracy of 0.99. These results contribute significantly to dental implant planning.

U-Net 3D architecture is also used for MC segmentation on AI-driven modules [15]. This study demonstrated a new, fast, and accurate AI-based module for MC segmentation in CBCT. However, studies that simultaneously and automatically detect AB and MC have not yet been widely established. Thus, there are many opportunities for accurate autodetection using deep learning to detect both objects.

YOLO, a state-of-the-art detection system based on deep learning, is a single-stage CNN detector that simultaneously makes object localization and classification predictions [19] with high detection accuracy and speed [8]. In object detection, many bounding boxes and their classifications must be drawn around the object. There are different versions of YOLO: YOLOv2 [20], YOLOv3 [21], and YOLOv4 [22]. To analyze medical images, YOLO was used to localize and track the myocardial wall from cardiac flow-field ultrasound images [23] and to automatically detect COVID-19 from raw chest X-ray images [24]. YOLOv3 was used to detect breast masses in full-field digital mammograms [25], and YOLOv4 was used to successfully detect melanoma lesions [26]. In dentistry, YOLOv3 has been successfully used to detect dental caries on digital bite radiographs [9], and YOLOv3-tiny has been successfully used to detect AB [27]. Therefore, YOLO is appropriate for dental implant planning, and in this case, for the simultaneous detection of AB and MC.

The YOLO detector consists of three main parts: backbone, neck, and head components. All object detectors take an image as input and compress the features down through the backbone of the CNN. In the neck, a combination of backbone features occurs in the layers. The head section detects an object by creating an object bounding box, predicting the object class, and determining the location of the object. YOLOv4 consists of a cross-stage partial (CSP) Darknet53 as the backbone network, spatial pyramid pooling (SPP) module, PANet as the neck network, and YOLOv3 as the head, which uses a three-scale feature map at the head to predict the detection results [22]. The CSP Darknet53 consists of a convolution building block (CBM) and five CSPResNet modules. The CBM contains a convolution layer (Conv), batch normalization layer, and Mish layer. CSPResNet is a convolutional neural network with a CSP approach that is applied to ResNet. Fig. 1 shows the YOLOv4 architecture. In the YOLOv4 architecture, three-scale feature maps (low, medium, and high) are used to detect objects of various sizes. In dental implant planning, simultaneous detection of AB and MC is required for the measurement of available bone in the implant area. AB can be easily detected because of its large size, whereas MC is more difficult to detect because of its small size. Detection using YOLOv4 to specifically detect AB and MC, which have large differences in size, may be less efficient. Therefore, it is crucial to provide appropriate feature maps on the YOLOv4 architecture to increase the detection efficiency of AB and MC.

This study proposes an automatic and simultaneous detection system for AB and MC based on 2D grayscale CBCT images that can simplify and expedite dental implant planning. We introduce Dental-YOLO, an efficient version of YOLOv4 specifically developed to detect AB and MC, with two-scale feature maps at low and high scales. A low-scale feature map is more efficient in detecting relatively large AB objects, whereas a high-scale feature map is more efficient at detecting much smaller MC objects. The detected bounding box attribute was then used to measure the available bone height and width in the implant area. The proposed detection system can produce bone quantity measurement, which is very important in dental implants.

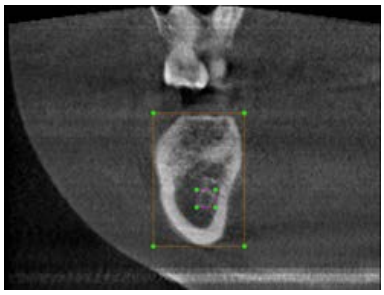

FIGURE 2. Annotation of the mandibular canal and alveolar bone on coronal slice.

TABLE 1. Distribution of the data.

Method	Total images	No. of annotations	
		AB	MC
Training	744	773	402
Testing	320	330	173
Total	**1064**	**1103**	**575**

II. METHODOLOGY

A. DATASETS

This study used 2D grayscales CBCT images of the coronal slices of the mandible. The images were annotated to create ground-truth images using LabelImg, a graphic annotation tool. The annotation process was performed by creating bounding boxes for each image's AB and MC objects. Fig. 2 shows an example of annotating AB and MC objects from the coronal slice. The AB annotations are depicted as a yellow box, and the MC annotations are depicted as a purple box. A text file in YOLO format for each image was generated containing the class number, center coordinate values, and the width and height of the bounding box relative to the image width and height for each object.

The CBCT dental images were obtained from Universitas Airlangga Academic Dental Hospital. All images were obtained using CBCT OP300 3D scanner (Instrumentarium Dental, Tuusula, Finland). The experiment used 1064 2D CBCT images of coronal slices, divided into 70% for training and 30% for testing. The training process used 744 images and 320 images for the testing process. 1678 annotations were made, consisting of 1103 AB and 575 MC annotations.

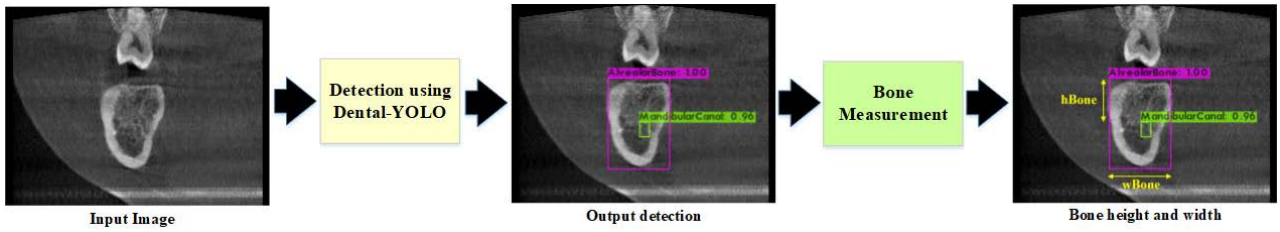

FIGURE 3. System workflow.

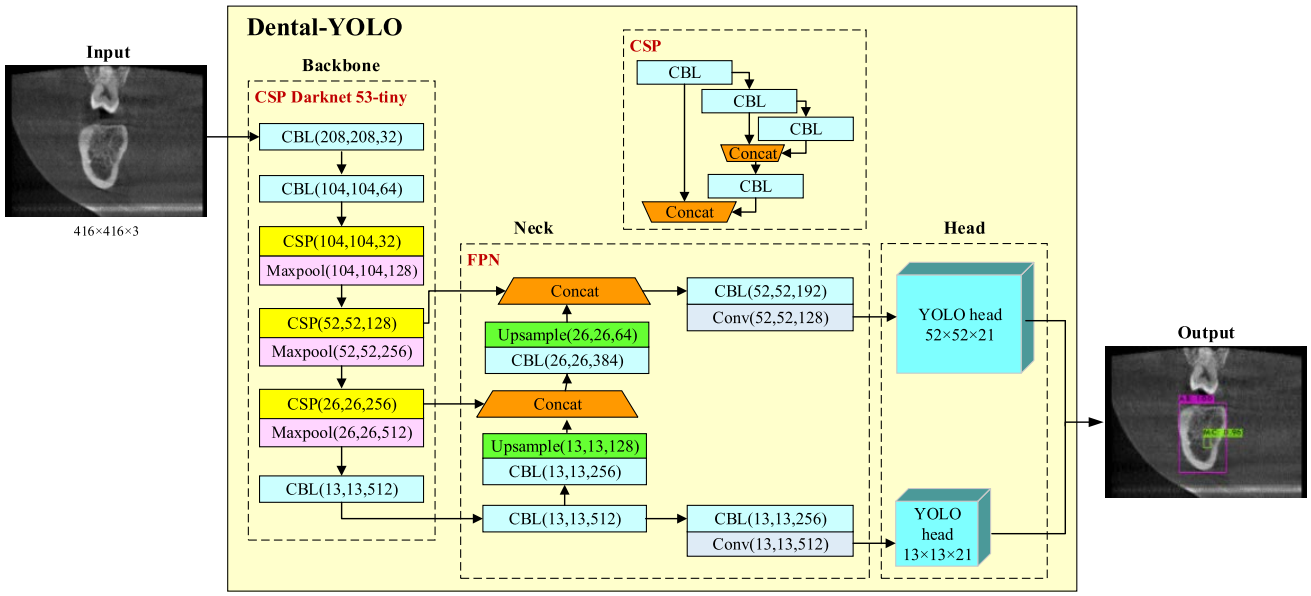

FIGURE 4. Dental-YOLO.

A radiologist with 14 years of professional experience validated the annotation results. Table 1 shows the distribution of the images and annotations used in this study.

B. SYSTEM OVERVIEW

To detect AB and MC objects, the image and ground truth that were developed are used as inputs to train and test Dental-YOLO. The Dental-YOLO model accepts an input image of size 416 × 416 pixels. Dental-YOLO training and testing used pre-prepared training and testing datasets. The detection results are shown as a bounding box, class name, and detection confidence value for the detected object. The class names used in this study were AB for the alveolar bone and MC for the mandibular canal. The detection confidence value ranges from 0.00 to 1.00, where 1.00 represents the highest level of detection confidence. The height and width of the available bone in the implant area were measured using the coordinates, length, and width of the bounding box obtained from Dental-YOLO detection. Fig. 3 shows the workflow of the system. The detection performance of Dental-YOLO was examined by comparing the detection results with those of a comparison detector. The measurements of bone height and width using the proposed approach were compared with the manual measurements conducted by two radiologists.

C. DENTAL-YOLO

The Dental-YOLO network model is specifically designed to detect AB and MC by making the YOLOv4 network model more efficient in the training and detection processes. Fig. 4 shows the Dental-YOLO architecture. Dental-YOLO uses a CSP Darknet53-tiny network as the backbone network. The CSP Darknet53-tiny consists of three convolution networks, batch normalization, LeakyReLU activation function (CBL) layers, and three CSP modules. The CSP Darknet53-tiny network uses the CSP module instead of the CSPResNet module used in CSP Darknet53. The CSP module can improve convolution network learning ability compared with the ResNet module [28]. The CSP network strategy reduces the computational complexity by dividing the feature map from the base layer into two parts and then combining them through a cross-stage hierarchy. In addition, CSPDarknet53-tiny uses the LeakyReLU activation function in the CSP module to simplify the computational process [28]. The maxpool layer is added after the CSP module

to maintain the resolution of the feature map. Simplification of this backbone network can lead to a faster training process. In the feature fusion section of the neck network, the Dental-YOLO approach uses a feature pyramid network (FPN) to extract feature maps with different scales. The FPN combines top-down path convolution networks and lateral connections to develop high-level semantic feature maps at all scales [29]. An FPN can enhance object detection speed with high detection accuracy. Dental-YOLO uses two-scale feature maps on the head to predict the detection results, making it more efficient in detecting two objects.

To better detect AB and MC, we used two-scale feature maps of low and high scales. Because AB objects can be detected easily owing to their relatively large size on CBCT images, the first branch of the Dental-YOLO output used a 13 × 13 low-scale feature map. MC is an object that is difficult to detect on CBCT images because it is small and sometimes invisible. Therefore, in this study, a 52 × 52 high-scale map feature was used to obtain better MC detection.

The Dental-YOLO detection process starts by dividing a 416 × 416 pixels input image into a grid size of 13 × 13. In each grid, three bounding boxes were generated to detect the objects. In each bounding box, a detection confidence value was generated to show the accuracy of the detection results for each object on the grid. The detection confidence value is zero if there are no objects in the grid. Otherwise, the detection confidence value is equal to the over union (*IoU*) intersection between the ground truth and bounding box. The confidence score threshold was used to determine which bounding box should be retained [21]. The bounding box with the highest detection confidence value is selected as the output of the detection process.

D. BONE HEIGHT AND WIDTH MEASUREMENT

The outputs of the detection process are the top-left coordinate (x, y) of the bounding box and the length and width of the object that can be detected in the image. The output values were used to calculate the height and width of available bone in the implant area. Bone height (*hBone*) is the distance between the crest of the bone and the MC [3]. In this study, *hBone* was calculated as the difference between the top y-coordinate value over the MC (top_yMC) and the top y-coordinate value over AB (top_yAB). An adjustment value for bone height (c_h) in millimeters was added to obtain *hBone* in line with the expert's calculations. The *hBone* equation proposed in this study is as in (1).

$$hBone = top_yMC - top_yAB + c_h \tag{1}$$

The alveolar process width determines the bone width (*wBone*) [4]. In this study, *wBone* was calculated from the width of the bounding box of AB (*widthAB*), as shown in (2). An adjustment value for bone width (c_w) in millimeters was added to obtain *wBone* in line with the expert's calculations.

$$wBone = widthAB + c_w \tag{2}$$

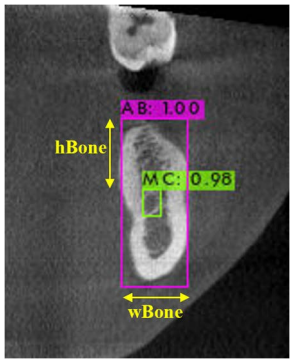

top_yMC = 105
top_yAB = 65
widthAB = 37 pixels
$c_h = c_w = 0$
hBone = 40 pixels = 12 mm
wBone = 37 pixels = 11.1 mm

FIGURE 5. Example of bone height and width measurement.

Fig. 5 shows an example of measuring *hBone* and *wBone* of the available bone using the result of the Dental-YOLO detection. *hBone* is calculated using (1) with $c_h = 0$, such that *hBone* is obtained from the difference between top_yMC and top_yAB, which is 40 pixels. *wBone* is calculated using (2) with $c_w = 0$, so *wBone* equals *widthAB*, which is 37 pixels. The image resolution is 0.3 × 0.3 × 0.3 mm, meaning that 1 pixel in the image file equals 0.3 mm.

III. EXPERIMENTS AND RESULTS

A. EXPERIMENTAL DESIGN

The training process was performed to develop a detection model using Dental-YOLO. This process used 744 annotated 2D coronal slice grayscale images. The training process was performed up to a maximum batch of 4000. The batch size, learning rate, momentum, and decay used in the experiment were 64, 0.001, 0.9, and 0.0005, respectively. After the detection model was developed, 320 images were used for testing. The output of the detection process is used for the bone measurement process.

In this study, four implant areas with varying AB morphology were selected for bone measurement. In each implant area, eleven images that measured the height and width of the available bone were selected. Image selection was based on the implant site area in relation to neighboring teeth and the mesial-distal width AB for the ideal dental implant location, which is 3 mm [30]. Since the pixel spacing is 0.3 mm, five images in the mesial direction and five images in the distal direction were taken from the center image of the implant site area, so that eleven images were selected for each implant area.

Two dental radiologists from the Airlangga University dental hospital performed manual bone measurements. The first radiologist, expert1, had 14 years of experience, while the expert2, had two years of experience. The two experts work individually and separately to take bone measurements using a CBCT viewer. The proposed approach measures bone using Equation 1 and 2, where previously the images were detected using Dental-YOLO. After measurement, the mean measurement of bone height and width in each implant area was calculated. These mean values were used to statistically

TABLE 2. Performance comparison of detection result.

Approach	AP AB (%)	AP MC (%)	mAP (%)	Avg IoU (%)	BFLOPS
YOLOv3	99.07	99.22	99.15	83.12	65.31
YOLOv3-tiny	99.04	96.12	97.58	78.50	**5.45**
YOLOv4	**99.68**	98.31	98.99	**84.51**	59.57
Dental-YOLO	99.37	**99.55**	**99.46**	81.33	6.83

AP AB, The average precision of AB detection; AP MC, The average precision of MC detection; mAP, mean average precision; avg IoU, average of intersection of union; BFLOPS, billions of floating-point operations.

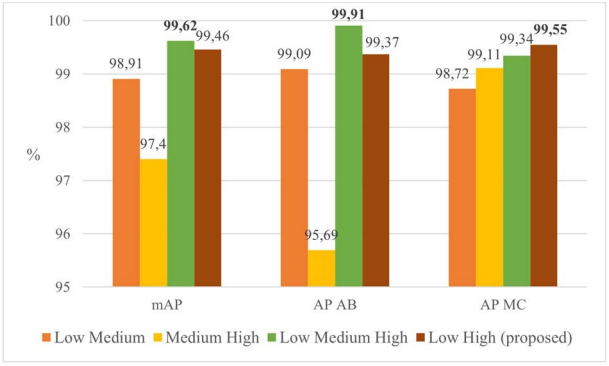

FIGURE 6. The detection performance with feature map scale variations on Dental-YOLO head.

compare the results of the two radiologists' bone measurements and the proposed method.

B. DETECTION PERFORMANCE

The algorithm's performance is compared with the other three algorithms: YOLOv4, YOLOv3, and YOLOv3-tiny. The metrics used in this experiment are *IoU*, the average precision (*AP*), and billions of floating-point operations (*BFLOPS*). The first two metrics, the *IoU* and *AP*, are used to measure the accuracy of the object detectors. The higher the *AP* and *IoU* values, the better the detection performance. In contrast, most recently, BFLOPS was used to measure the computational time complexity of the number of model operations. The lower the BFLOPS value, the better the performance, which means the algorithm requires lower computing power to conduct the training process.

From Table 2, we can see that in terms of AP, Dental-YOLO outperforms all of the other algorithms having the highest value of mean average precision (*mAP*) of 99.46 percent. Note that *mAP* is the mean of *AP* of class AB and *AP* of MC. Even though the average IoU of Dental-YOLO is 81.33 percent, slightly lower than YOLOv3 and YOLOv4 having an average *IoU* of 83.12 and 84.51, respectively, Dental-YOLO is eight times faster than YOLOv4. In terms of computational power, Dental-YOLO's performance is comparable with the most efficient algorithm, YOLOv3-tiny. Note that Dental-YOLO significantly outperformed YOLOv3-tiny in both mAP and Avg IoU. Dental-YOLO is proven to be an algorithm with efficient computational power without sacrificing detection accuracy.

The efficiency of Dental-YOLO is reached via architecture simplification from the previous work, like YOLOv4, where it can significantly reduce the *BFLOPS* required from 59.57 to 6.83, making the training process faster. The architecture simplification of Dental-YOLO and YOLOv3-tiny uses two feature maps in the output branch. Therefore, *BFLOPS* of Dental-YOLO and YOLOv3tiny are smaller than the other two algorithms, YOLOv3 and YOLOv4. Note that the size of the backbone network in Dental-YOLO is slightly more complex than that in YOLOv3-tiny, resulting in the *BFLOPS* of Dental-YOLO being slightly larger than that of YOLOv3-tiny. The overall detection result of the proposed approach, Dental-YOLO, is better than that of the YOLOv3-tiny approach.

A comparison of the detection performance was performed by changing the combination of the feature map scales on the Dental-YOLO head. The scale variations carried out are low and medium scale, medium and high scale, as well as a combination of low, medium, and high scales. The results of the detection of variations in the scale were compared with the low and high scales used in this study. Fig. 6 shows the detection performance results obtained using feature map scale variations on Dental-YOLO heads. The low and high scales used in the proposed Dental-YOLO architecture achieved the best results in MC detection, with an AP MC of 99.55%. While the use of low and medium scales resulted in the lowest MC detection compared to other scale variations. These results indicate that high-scale feature maps are more suitable for MC detection. The use of low and high scales in the proposed Dental-YOLO architecture resulted in slightly lower mAP and AP AB values than using all scales (low, medium, and high). However, using two scales in Dental-YOLO is more efficient than using three scales. For AB detection results, the use of medium and high scales produces the lowest mAP and AP values compared to other combinations that use low scales. This indicates that the combination of medium and high scale is not suitable for detecting AB. This shows that AB can be recognized well with a low scale.

Fig. 7 shows examples of the AB and MC detection results using Dental-YOLO with variations in the shape and number of AB and MC. The image shows the detection results in the form of a bounding box on the AB and MC that were successfully detected, and the detection confidence value was written above the bounding box. All AB objects in the sample were detected successfully, with a high confidence measurement because the size of AB was quite large and visible. For MC detection, the confidence value of the detection results depends on the clarity of the MC image. If it is clear, the confidence value is high (above 0.9), as shown in Fig. 7(a), (b), (c) on the right, and (d) on the left, the MC is a small sphere in AB. The MC is less clear in Fig. 7(c) on the left. Therefore, the confidence value is only 0.65. Meanwhile,

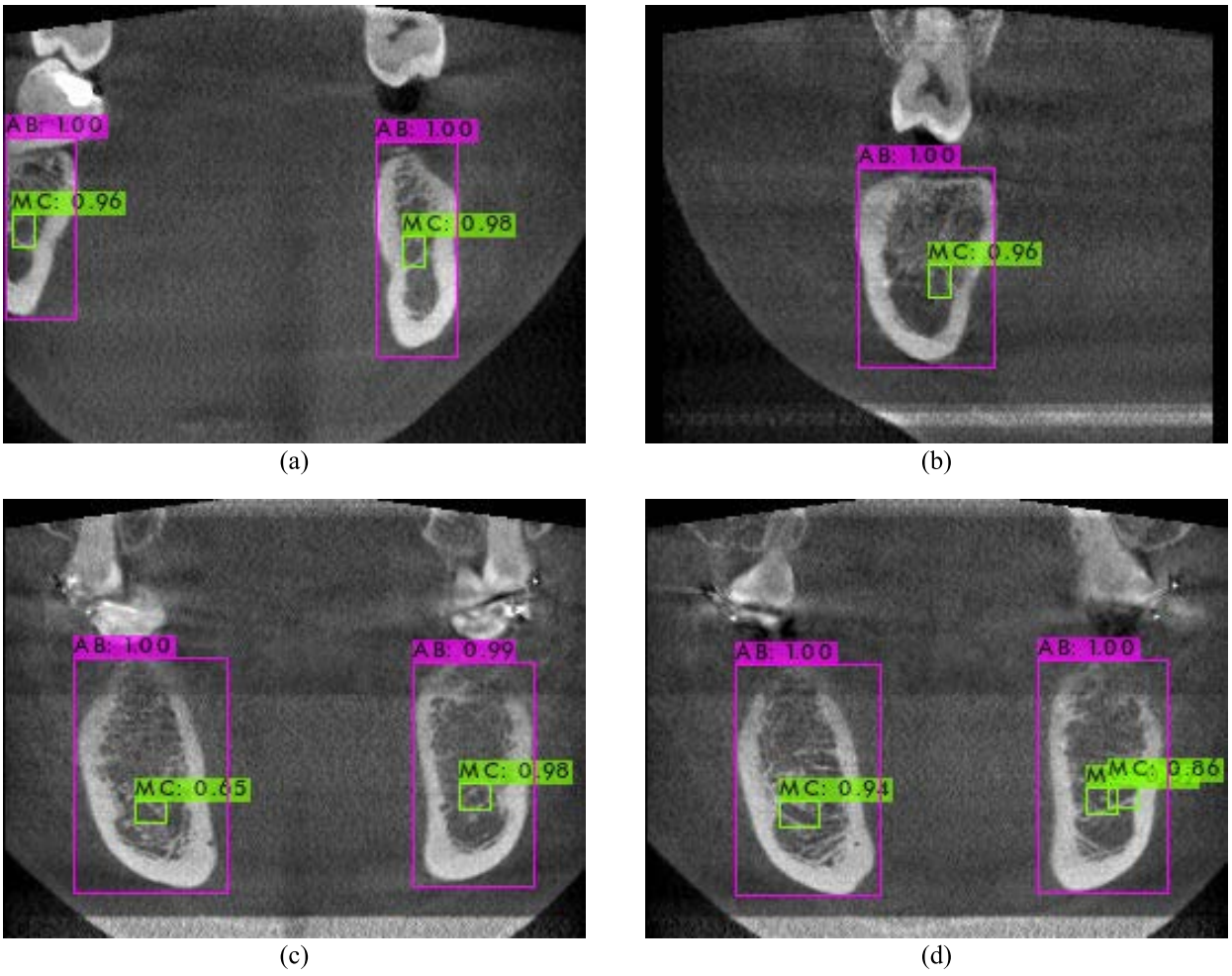

FIGURE 7. Examples of detection results using Dental-YOLO; (a) and (b) high confidence value in detecting AB and MC, (c) low confidence value for left MC detection, (d) false positive in detecting right MC.

in Fig. 7(d), there is a false-positive case in detecting the MC in the right bone as two adjacent MC objects. This is because the shape of the MC elongated from walls AB and inside AB.

The study detected AB using YOLOv3-tiny, resulting in *mAP* of 98.60% [27]. The difference between YOLOv3-tiny and Dental-YOLO lies in the backbone architecture; YOLOv3 uses Darknet53, whereas Dental-YOLO uses CSPDarknet. The use of CSP modules can improve the learning ability of convolution networks and increase their accuracy. Dental-YOLO achieved *AP* of 94.97% for AB detection, outperforming YOLOv3-tiny.

C. BONE MEASUREMENT

The *hBone* and *wBone* measurements of the proposed approach (*P*) were calculated using equations (1) and (2) and compared with the measurements made in expert1 (*E1*) and expert2 (*E2*). Table 3 shows the mean height (*Mh*) and mean width (*Mw*), as well as the difference in mean height (*MDh*) and difference in mean width (*MDw*) of the four bone implant areas. The mean difference (MD) was calculated from the difference in the mean measurement between the experts (*MDhE* and *MDwE*) and the difference in the mean measurement between the expert and the proposed approach (*MDhE1P, MDhE2P, MDwE1P*, and *MDwE2P*). The MD column for each height and width measurement also displayed the smallest value (*min*), largest value (*max*), and range between the smallest and largest MD values (*range*). In this study, the c_h value for the *hBone* measurement was -1, and the c_w for the *wBone* measurement was -0.3.

Table 3 shows MD among experts was small for measurements of bone height (*MDhE*) and width (*MDwE*). The *range* of MD indicates that the measurement of bone height has a smaller MD than that of bone width.

D. STATISTICAL ANALYSIS

Bone measurements were evaluated by two-way ANOVA using the Minitab 19. Two-way ANOVA was performed to test whether there was a difference in the measurement between the proposed approach and the experts. Two independent variables were analyzed for their significance in the measurement of mean bone height and width. The first

TABLE 3. Mean and mean difference (MD) in bone height and width measurements.

	Mean bone height (mm)						Mean bone width (mm)					
Implant area	*MhE1*	*MhE2*	*MhP*	*MDhE*	*MDhE1P*	*MDhE2P*	*MwE1*	*MwE2*	*MwP*	*MDwE*	*MDwE1P*	*MDwE2P*
1	10.99	10.98	10.89	**0.01**	0.10	**0.09**	11.36	11.13	11.26	0.23	**0.10**	**0.13**
2	11.66	11.51	12.64	0.15	0.98	1.13	18.81	18.64	18.33	0.17	0.48	0.31
3	17.02	16.83	17.05	0.19	**0.03**	0.22	14.86	14.71	17.75	0.15	2.89	3.04
4	16.38	16.28	16.54	0.10	0.16	0.26	15.43	15.37	19.88	**0.06**	4.45	4.51
min				0.01	0.03	0.09				0.06	0.10	0.13
max				0.19	0.98	1.13				0.23	4.45	4.51
range				0.18	0.95	1.04				0.17	4.35	4.38

MhE1,The mean height measurement by expert1; MhE2, The mean height measurement by expert2; MhP,The mean height measurement by proposed approach; MDhE, The mean difference of bone height measurement between experts, MDhE1P, The mean difference of bone height measurement between expert1 and proposed approach; MDhE2P, The mean difference of bone height measurement between expert2 and proposed approach; MwE1, The mean width measurement by expert1; MwE2, The mean width measurement by expert2; MwP, The mean width measurement by proposed approach; MDwE, The mean difference of bone width measurement between experts; MDwE1P, The mean difference of bone width measurement between expert1 and proposed approach; MDwE2P, The mean difference of bone width measurement between expert2 and proposed approach.

TABLE 4. Result of two-way ANOVA for bone height measurements.

Source	DF	Adj SS	Adj MS	F-value	P-va
System	2	0.305	0.152	1.77	**0.2**
plant area	3	84.254	28.084	325.69	**0.0**
Error	6	0.517	0.086		
Total	11	85.075			

TABLE 5. Result of two-way ANOVA for bone width measurements.

Source	DF	Adj SS	Adj MS	F-value	P-value
System	2	8.367	4.183	2.27	**0.184**
Implant area	3	88.747	29.582	16.09	**0.003**
Error	6	11.034	1.839		
Total	11	108.146			

TABLE 6. Grouping information using the Tukey method for measuring bone height.

Implant area	N	Mean	Grouping
3	3	16.967	**A**
4	3	16.400	**A**
2	3	11.937	**B**
1	3	10.953	**C**

TABLE 7. Grouping information using the Tukey method for measuring bone width.

Implant area	N	Mean	Grouping
2	3	18.593	**A**
4	3	16.893	**A**
3	3	15.773	**A**
1	3	11.250	**B**

variable is the *system*, which is the object that takes the measurements and consists of the proposed approach, expert1, and expert2. The second variable is the *implant area*, which comprises four implant areas where measurements are taken, namely implant areas 1, 2, 3, and 4. Fig. 8 shows bones with various AB morphology variations from each implant area.

Tables 4 and 5 show the results of the two-way ANOVA test for the measurement of bone height and width, respectively, from Minitab19. The significance level (α) used in the two-way ANOVA test was 0.05. For the *system* variable, the p-value obtained from the measurement of bone height was 0.249, and that of bone width was 0.184, both of which were greater than 0.05. This means that the *system* variable had no significant effect on the bone height and width measurements. It can be concluded that there is no difference in the measurement of bone height and width produced by the proposed approach and experts. As for the *implant area* variable, the p-value of bone height measurement was 0.000 and bone width measurement was 0.003, both of which were smaller than 0.05. This means that the *implant area* variable significantly affects the measurement of the bone height and width.

Analysis after the two-way ANOVA was performed for variables with p-values ≤ 0.05. Tukey's test was used to determine the *implant area* variable group based on mean bone height and width. Tables 6 and 7 show the grouping information using Tukey's analysis for measuring bone height and width from Minitab 19. From the information on the implant area group for measuring bone height, implant areas 3 and 4 were in the same group, whereas areas 2 and 1 were in separate groups. Meanwhile, the group information for measuring bone width showed that implant areas 2, 4, and 3 were in the same group, and area 1 was in another group.

The results of the two-way ANOVA test showed that there was no difference in bone height and width measurements produced by the proposed approach and the experts. This indicates that the proposed approach can be used to measure the available bone in the implant area. This means that the bounding box attribute of AB and MC detection from Dental-YOLO can be used for bone measurement in dental implant planning.

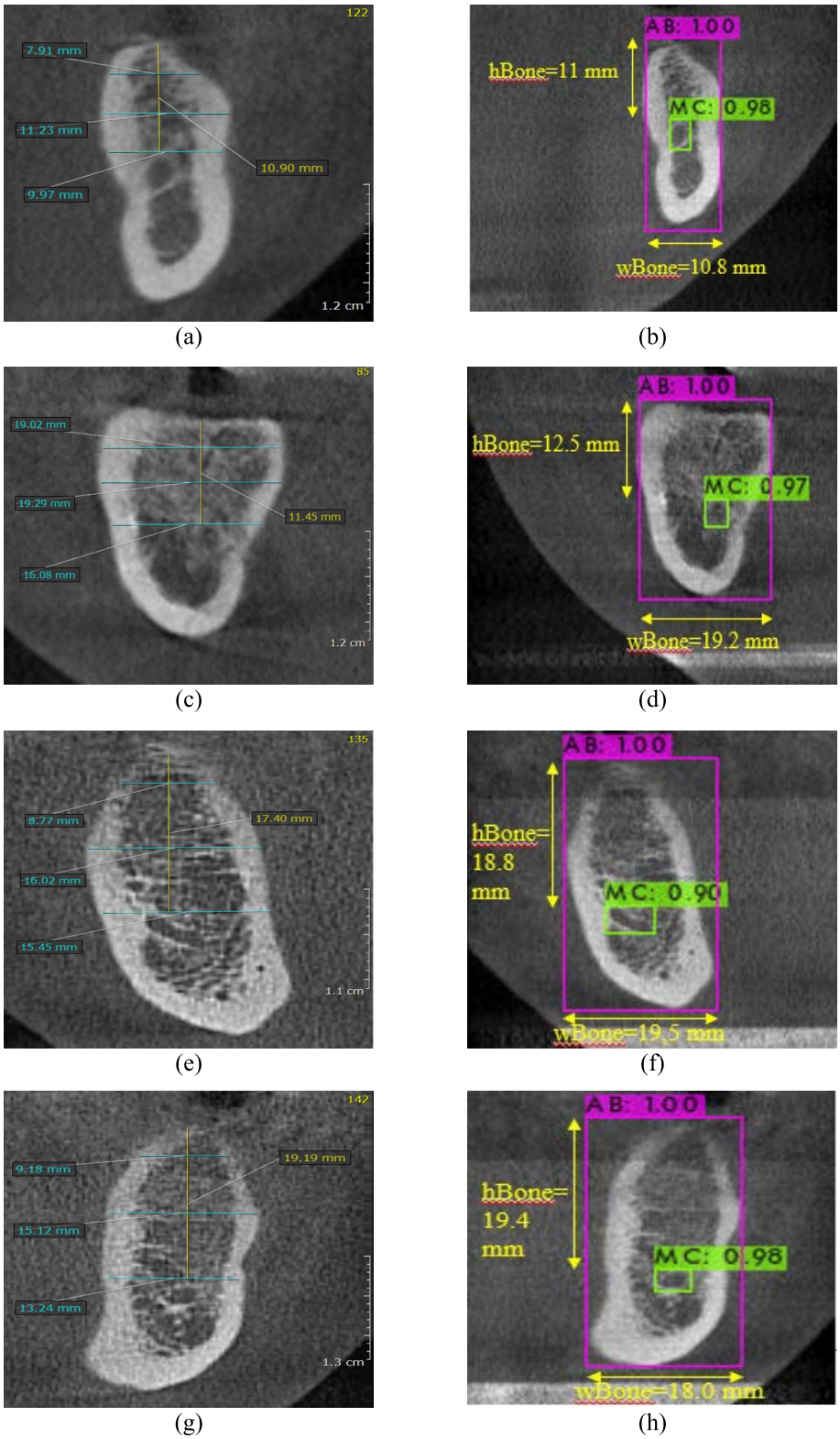

FIGURE 8. Height and width bone measurement by expert1 and proposed approach; (a) and (b) implant area 1-region 36, (c) and (d) implant area 2-region 47, (e) and (f) implant area 3-region 46, (g) and (h) implant area 4–region 36.

However, the implant area affects the measurement of bone height and width. This is due to the different morphologies of AB in the measured implant area. Fig. 8 displays the bone measurement results for four implant areas with varying

AB morphology from expert1 and the proposed approach. AB in implant areas 3 and 4 had a similar bone morphology to the bone in areas 1 and 2. Implant areas 3 and 4 were in the same group, based on the grouping results for bone height and width. Implant area 1 has AB, which is narrower in width than other implant areas; therefore, it is in a separate group in the measurement of bone width. The bone measurements shown in Table 3 indicate that the MD bone height in implant area 1 was the smallest. The bone crest of implant area 1 was not reduced, and the bone position was upright so that the bone crest was at the top of the bounding box. Fig. 8(a) shows the expert1 *hBone* measurement at area 1 of 10.90 mm. Fig. 8(b) shows the *hBone* of the proposed approach of 11 mm. The measurement difference was 0.1 mm. In contrast, the MD bone height in implant area 2 was the highest. Fig. 8(c) and (d) show 2D CBCT images in the implant area 2. In these images, the bone crest decreased owing to bone loss. The top of the bone area was below the top of the bounding box AB. Fig. 8(c) shows the expert1 *hBone* measurement in area 2 of 11.45 mm and (d) shows the proposed approach of 12.5 mm. The measurement difference was 1.05 mm. A decrease in the AB bone peak affected the *hBone* measurement value.

Three measurements were performed by each expert to determine the available bone width. The experts chose the largest of the three bone width measurements as *wBone*. Fig. 8(a) shows the *wBone* value obtained by expert1 of 11.23 mm. The proposed *wBone* measurement in this study measures the width of AB from the width of the bounding box AB. Fig. 8(b) shows the *wBone* value of 10.8 mm. Table 3 shows that in the measurement of bone width, the MD in width for implants 1 and 2 is less than 1 mm, while the area for implants 3 and 4 is more than 3 mm. Fig. 8(a) to (d) show 2D CBCT images for implant areas 1 and 2. As shown in the figure, the AB bones are in an upright position such that the measured available bone width corresponds to the width of the AB bounding box. The width measurements were similar to the expert measurements. Fig. 8(e) to (h) show images of the implant areas 3 and 4, respectively. In the pictures, it can be seen that the shape of AB is not perpendicular. Therefore, the width of the bounding box AB is larger than the actual bone width. This causes the bone width measurement of the proposed approach to be larger than that of expert measurement.

Further research is needed to measure the height and width of the AB more precisely to reduce the MD in the bone height and width. AB crest detection can be applied to obtain a more precise *hBone,* especially in bones with decreased AB crest. The AB segmentation process can be applied to obtain a more precise *wBone* size, with the *wBone* measurement performed from the edge of AB.

IV. CONCLUSION

Dental-YOLO is a compressed version of YOLOv4 that successfully detects AB and MC simultaneously, using low- and high-scale features. Dental-YOLO has an average detection precision of 99.46%. Dental-YOLO detection was eight times faster than that using the YOLOv4 approach. Dental-YOLO's *BFLOPS* was 6.83, which was significantly smaller than that of YOLOv4's *BFLOPS* of 59.57. The training process becomes much more efficient. This greatly helps the efficiency of the development of the Dental-YOLO system in implant treatment planning.

The ANOVA test, which analyzes the comparison between the measurement results by the system and the radiologists, shows that automatic AB and MC detection can be used to properly measure the available bone in the implant area. There was shown to be no significant difference between the radiologist's measurements and the proposed method. Therefore, automated measurements can be used to simplify dental implant planning. However, further research is needed to improve the accuracy of bone measurement through the detection of AB crest and segmentation of the AB on dental CBCT images.

REFERENCES

[1] M. Bae, J.-W. Park, and N. Kim, "Fully automated estimation of arch forms in cone-beam CT with cubic B-spline approximation: Evaluation of digital dental models with missing teeth," *Comput. Biol. Med.*, vol. 131, Apr. 2021, Art. no. 104256, doi: 10.1016/j.compbiomed.2021.104256.

[2] P. Worthington, J. Rubenstein, and D. C. Hatcher, "The role of cone-beam computed tomography in the planning and placement of implants," *J. Amer. Dental Assoc.*, vol. 141, pp. 19S–24S, Oct. 2010, doi: 10.14219/jada.archive.2010.0358.

[3] R. Jacobs, B. Salmon, M. Codari, B. Hassan, and M. M. Bornstein, "Cone beam computed tomography in implant dentistry: Recommendations for clinical use," *BMC Oral Health*, vol. 18, no. 1, pp. 1–17, Dec. 2018, doi: 10.1186/s12903-018-0523-5.

[4] G. Juodzbalys and M. Kubilius, "Clinical and radiological classification of the jawbone anatomy in endosseous dental implant treatment," *J. Oral Maxillofacial Res.*, vol. 4, no. 2, pp. 1–17, 2013, Art. no. e2, doi: 10.5037/jomr.2013.4202.

[5] M.-L. Sun, Y. Liu, G. Liu, D. Cui, A. A. Heidari, W.-Y. Jia, X. Ji, H. Chen, and Y. Luo, "Application of machine learning to stomatology: A comprehensive review," *IEEE Access*, vol. 8, pp. 184360–184374, 2020, doi: 10.1109/ACCESS.2020.3028600.

[6] J. Jaskari, J. Sahlsten, J. Järnstedt, H. Mehtonen, K. Karhu, O. Sundqvist, A. Hietanen, V. Varjonen, V. Mattila, and K. Kaski, "Deep learning method for mandibular canal segmentation in dental cone beam computed tomography volumes," *Sci. Rep.*, vol. 10, no. 1, pp. 1–9, Dec. 2020, doi: 10.1038/s41598-020-62321-3.

[7] R. H. Putra, C. Doi, N. Yoda, E. R. Astuti, and K. Sasaki, "Current applications and development of artificial intelligence for digital dental radiography," *Dentomaxillofacial Radiol.*, vol. 51, no. 1, pp. 1–12, 2022, doi: 10.1259/dmfr.20210197.

[8] X. Hu, Y. Liu, Z. Zhao, J. Liu, X. Yang, C. Sun, S. Chen, B. Li, and C. Zhou, "Real-time detection of uneaten feed pellets in underwater images for aquaculture using an improved YOLO-V4 network," *Comput. Electron. Agricult.*, vol. 185, Jun. 2021, Art. no. 106135, doi: 10.1016/j.compag.2021.106135.

[9] Y. Bayraktar and E. Ayan, "Diagnosis of interproximal caries lesions with deep convolutional neural network in digital bitewing radiographs," *Clin. Oral Investigations*, vol. 26, no. 1, pp. 623–632, Jan. 2022, doi: 10.1007/s00784-021-04040-1.

[10] H.-J. Chang, S.-J. Lee, T.-H. Yong, N.-Y. Shin, B.-G. Jang, J.-E. Kim, K.-H. Huh, S.-S. Lee, M.-S. Heo, S.-C. Choi, T.-I. Kim, and W.-J. Yi, "Deep learning hybrid method to automatically diagnose periodontal bone loss and stage periodontitis," *Sci. Rep.*, vol. 10, no. 1, pp. 1–9, Dec. 2020, doi: 10.1038/s41598-020-64509-z.

[11] Y. Miki, C. Muramatsu, and T. Hayashi, "Classification of teeth in cone-beam CT using deep convolutional neural network," *Comput. Biol. Med.*, vol. 80, pp. 24–29, Jan. 2017, doi: 10.1016/j.compbiomed.2016.11.003.

[12] Z. Cui, Y. Fang, L. Mei, B. Zhang, B. Yu, J. Liu, C. Jiang, Y. Sun, L. Ma, J. Huang, Y. Liu, Y. Zhao, C. Lian, Z. Ding, M. Zhu, and D. Shen, "A fully automatic AI system for tooth and alveolar bone segmentation from cone-beam CT images," *Nature Commun.*, vol. 13, no. 1, pp. 1–11, Dec. 2022, doi: 10.1038/s41467-022-29637-2.

[13] R. Indraswari, A. Arifin, N. Suciati, E. Astuti, and T. Kurita, "Automatic segmentation of mandibular cortical bone on cone-beam CT images based on histogram thresholding and polynomial fitting," *Int. J. Intell. Eng. Syst.*, vol. 12, no. 4, pp. 130–141, Aug. 2019, doi: 10.22266/ijies2019.0831.13.

[14] G. H. Kwak, E.-J. Kwak, J. M. Song, H. R. Park, Y.-H. Jung, B.-H. Cho, P. Hui, and J. J. Hwang, "Automatic mandibular canal detection using a deep convolutional neural network," *Sci. Rep.*, vol. 10, no. 1, pp. 1–9, Dec. 2020, doi: 10.1038/s41598-020-62586-8.

[15] P. Lahoud, S. Diels, L. Niclaes, S. Van Aelst, H. Willems, A. Van Gerven, M. Quirynen, and R. Jacobs, "Development and validation of a novel artificial intelligence driven tool for accurate mandibular canal segmentation on CBCT," *J. Dentistry*, vol. 116, Jan. 2022, Art. no. 103891, doi: 10.1016/j.jdent.2021.103891.

[16] S. Lee, S. Woo, J. Yu, J. Seo, J. Lee, and C. Lee, "Automated CNN-based tooth segmentation in cone-beam CT for dental implant planning," *IEEE Access*, vol. 8, pp. 50507–50518, 2020, doi: 10.1109/ACCESS.2020.2975826.

[17] R. Indraswari, T. Kurita, A. Z. Arifin, N. Suciati, and E. R. Astuti, "Multi-projection deep learning network for segmentation of 3D medical images," *Pattern Recognit. Lett.*, vol. 125, pp. 791–797, Jul. 2019, doi: 10.1016/j.patrec.2019.08.003.

[18] H.-K. Lim, S.-K. Jung, S.-H. Kim, Y. Cho, and I.-S. Song, "Deep semi-supervised learning for automatic segmentation of inferior alveolar nerve using a convolutional neural network," *BMC Oral Health*, vol. 21, no. 1, pp. 1–9, Dec. 2021, doi: 10.1186/s12903-021-01983-5.

[19] J. Redmon, S. Divvala, R. Girshick, and A. Farhadi, "You only look once: Unified, real-time object detection," in *Proc. IEEE Conf. Comput. Vis. Pattern Recognit. (CVPR)*, Jun. 2016, pp. 779–788, doi: 10.1109/CVPR.2016.91.

[20] J. Redmon and A. Farhadi, "YOLO9000: Better, faster, stronger," in *Proc. IEEE Conf. Comput. Vis. Pattern Recognit. (CVPR)*, Jul. 2017, pp. 6517–6525, doi: 10.1109/CVPR.2017.690.

[21] J. Redmon and A. Farhadi, "YOLOv3: An incremental improvement," 2018, *arXiv:1804.02767*.

[22] A. Bochkovskiy, C.-Y. Wang, and H.-Y. M. Liao, "YOLOv4: Optimal speed and accuracy of object detection," 2020, *arXiv:2004.10934*.

[23] Z. Zhuang, G. Liu, W. Ding, A. N. J. Raj, S. Qiu, J. Guo, and Y. Yuan, "Cardiac VFM visualization and analysis based on YOLO deep learning model and modified 2D continuity equation," *Computerized Med. Imag. Graph.*, vol. 82, Jun. 2020, Art. no. 101732, doi: 10.1016/j.compmedimag.2020.101732.

[24] T. Ozturk, M. Talo, E. A. Yildirim, U. B. Baloglu, O. Yildirim, and U. R. Acharya, "Automated detection of COVID-19 cases using deep neural networks with X-ray images," *Comput. Biol. Med.*, vol. 121, Jun. 2020, Art. no. 103792, doi: 10.1016/j.compbiomed.2020.103792.

[25] G. H. Aly, M. Marey, S. A. El-Sayed, and M. F. Tolba, "YOLO based breast masses detection and classification in full-field digital mammograms," *Comput. Methods Programs Biomed.*, vol. 200, Mar. 2021, Art. no. 105823, doi: 10.1016/j.cmpb.2020.105823.

[26] S. Albahli, N. Nida, A. Irtaza, M. H. Yousaf, and M. T. Mahmood, "Melanoma lesion detection and segmentation using YOLOv4-DarkNet and active contour," *IEEE Access*, vol. 8, pp. 198403–198414, 2020, doi: 10.1109/ACCESS.2020.3035345.

[27] M. Widiasri, A. Z. Arifin, N. Suciati, E. R. Astuti, and R. Indraswari, "Alveolar bone detection from dental cone beam computed tomography using YOLOv3-tiny," in *Proc. Int. Conf. Artif. Intell. Mechatronics Syst. (AIMS)*, Apr. 2021, pp. 1–6, doi: 10.1109/aims52415.2021.9466037.

[28] P. Xu, Q. Li, B. Zhang, F. Wu, K. Zhao, X. Du, C. Yang, and R. Zhong, "On-board real-time ship detection in HISEA-1 SAR images based on CFAR and lightweight deep learning," *Remote Sens.*, vol. 13, no. 10, pp. 1–18, 2021, doi: 10.3390/rs13101995.

[29] X. Li, T. Lai, S. Wang, Q. Chen, C. Yang, R. Chen, J. Lin, and F. Zheng, "Weighted feature pyramid networks for object detection," in *Proc. IEEE Int. Conf. Parallel Distrib. Process. Appl., Big Data Cloud Comput., Sustain. Comput. Commun., Social Comput. Netw. (ISPA/BDCloud/SocialCom/SustainCom)*, Dec. 2019, pp. 1500–1504, doi: 10.1109/ISPA-BDCloud-SustainCom-SocialCom48970.2019.00217.

[30] A. Cristoforetti, L. De Stavola, A. Fincato, M. Masè, F. Ravelli, G. Nollo, and F. Tessarolo, "Assessing the accuracy of computer-planned osteotomy guided by stereolithographic template: A methodological framework applied to the mandibular bone harvesting," *Comput. Biol. Med.*, vol. 114, Nov. 2019, Art. no. 103435, doi: 10.1016/j.compbiomed.2019.103435.

MONICA WIDIASRI (Member, IEEE) received the bachelor's and master's degrees in computer science from the Institut Teknologi Sepuluh Nopember, in 2001 and 2012, respectively, where she is currently pursuing the Ph.D. degree. She has also been a Lecturer with Universitas Surabaya, since 2003. Her research interests include artificial intelligence, deep learning, computer vision, and pattern recognition.

AGUS ZAINAL ARIFIN received the bachelor's degree in computer science from the Institut Teknologi Sepuluh Nopember, in 1995, the master's degree in computer science from Universitas Indonesia, in 2001, and the Ph.D. degree in information engineering from Hiroshima University, in 2007. He has been a Lecturer with the Department of Informatics, Institut Teknologi Sepuluh Nopember, since 1995. He is among the top 500 authors based on the SINTA Score 2020. His research interests include image processing, particularly in medical imaging, machine learning, deep learning, and information retrieval. Since May 2021, he has been the Head of the Center for Social Welfare Data and Information of the Ministry of Social Affairs of the Republic of Indonesia.

NANIK SUCIATI (Member, IEEE) received the master's degree in computer science from the University of Indonesia, in 1998, and the Dr.Eng. degree in information engineering from the University of Hiroshima, in 2010. She is currently an Associate Professor with the Department of Informatics, Institut Teknologi Sepuluh Nopember. She has published more than 50 journal articles and conference papers on computer science. Her research interests include computer vision, computer graphics, and artificial intelligence.

CHASTINE FATICHAH (Member, IEEE) received the Ph.D. degree from the Tokyo Institute of Technology, Japan, in 2012. She is currently an Associate Professor with the Institut Teknologi Sepuluh Nopember, Surabaya, Indonesia. She has published more than 110 journal articles and conference papers related to computer science. Her research interests include artificial intelligence, image processing, and data mining.

EHA RENWI ASTUTI received Ph.D. degree in health science from the Faculty of Medicine Post-Graduate Course, Universitas Airlangga, Indonesia, in 2005. She is currently an Associate Professor with the Department of Dentomaxillofacial Radiology, Universitas Airlangga, Indonesia. Since 2008, she has been working as an Oral Radiologist with Universitas Airlangga Academic Dental Hospital, Indonesia. Her research interests include radiographic imaging, artificial intelligence in dental radiography, radioprotective agents, radiology in forensic odontology, and radiation biology.

RARASMAYA INDRASWARI (Member, IEEE) received the bachelor's degree in computer science from the Institut Teknologi Sepuluh Nopember, in 2015, the integrated master's and Ph.D. degree from the Ministry of Higher Education, Indonesia, to take the doctoral degree directly, with PMDSU (master-to-doctoral program for excellent undergraduate) scholarship, and the Ph.D. degree in computer science from the Institut Teknologi Sepuluh Nopember, in March 2020. She is currently a Lecturer with the Department of Information Systems, Institut Teknologi Sepuluh Nopember. Her research interests include data mining, machine learning, image processing, and computer vision.

RAMADHAN HARDANI PUTRA received the Ph.D. degree in dental science from the Graduate School of Dentistry, Tohoku University, Japan, in 2021. He is currently a Lecturer with the Department of Dentomaxillofacial Radiology, Universitas Airlangga, Indonesia. His research interests include dental implant, digital dentistry, radiographic imaging, and artificial intelligence in dental radiography.

CHOIRU ZA'IN received the Ph.D. degree from the School of Computing, Engineering, and Mathematical Science, La Trobe University, Melbourne, in 2020. He is with Monash University as a Research Associate and a Sessional Lecturer with the Faculty of Information Technology. His research interest includes large-scale data stream analysis, and he has published in many high-quality journals in computer science. He has also been involved in reviewing many reputable journals.